Microstructural characterisation of a Ni–Fe-based superalloy by *in situ* small-angle neutron scattering measurements

2008 J. Phys.: Condens. Matter 20 104220

(http://iopscience.iop.org/0953-8984/20/10/104220)

J. Phys.: Condens. Matter **20** (2008) 104220 (9pp) doi:10.1088/0953-8984/20/10/104220

Microstructural characterisation of a Ni–Fe-based superalloy by *in situ* small-angle neutron scattering measurements

D Mukherji[1], D Del Genovese[1], P Strunz[2,3], R Gilles[4], A Wiedenmann[5] and J Rösler[1]

[1] TU Braunschweig, IfW, Langer Kamp 8, D-38106 Braunschweig, Germany
[2] Nuclear Physics Institute and Research Centre Řež, CZ-25068 Řež near Prague, Czech Republic
[3] LNS, PSI & ETHZ, CH-5232 Villigen Paul Scherrer Institute, Switzerland
[4] TU München, Forschungsneutronenquelle Heinz Maier-Leibnitz (FRM II), ZWE Lichtenbergstraße 1, D-85747 Garching, Germany
[5] Hahn-Meitner-Institute Berlin, Glienickerstraße 100, D-14109 Berlin, Germany

E-mail: d.mukherji@tu-bs.de

Received 16 July 2007
Published 19 February 2008
Online at stacks.iop.org/JPhysCM/20/104220

Abstract

The microstructural evolution at high temperatures was studied in an experimental Ni–Fe-based superalloy DT706 by *in situ* small-angle neutron scattering (SANS). Modifying the alloy heat treatment to improve the microstructural stability and mechanical properties in Inconel 706 type superalloys has been a significant research goal for many years. The earlier studies of phase transformation relied mostly on optical and electron microscopy investigations of samples that were cooled down to room temperature after the high-temperature exposure. However, the kinetics of γ' and γ'' precipitation is very fast and new precipitation does occur during the cooling phase. So it is unlikely that the high-temperature microstructure is retained at room temperature. In this presentation, we followed the phase transformation in DT706 alloy by studying the microstructural changes occurring at elevated temperatures. The results of *in situ* SANS measurements are presented. Microstructure examination on differently heat-treated samples by electron microscopy gives complementary information on the phase transformation sequences. The formation and evolution of precipitates are strongly influenced by the cooling rate from the solution to the η stabilization temperature. The microstructure of DT706 alloy can be tuned using the *in situ* SANS results.

(Some figures in this article are in colour only in the electronic version)

1. Introduction

The development of new generation steam turbines for use in advanced coal-fired power plants operating at higher temperatures can reduce CO_2 emission and increase energy efficiency. To fulfil this goal the objective of the European 'THERMIE advanced pulverised fuel (PF) power plant' project is to develop ultra-supercritical steam turbines achieving an efficiency of up to 55% with approximately 400 MW and the steam parameters 700–720 °C/350 bar. Compared with a coal-fired power plant with an efficiency of 35%, this will yield a reduction in greenhouse gases by roughly 30%. Present coal-fired plants have reached an efficiency of 45%. However, the technical and economic feasibility of this development concept fundamentally relies on the application of nickel-based alloys to enable the high (700–720 °C) steam temperatures. The commercial alloy Inconel 706 was a candidate, but was found to be unstable for application at these high temperatures [1].

Table 1. List of samples for *in situ* SANS measurements (at HMI and at PSI).

Sample No.	Solution treatment T_{sol}, time (°C), (h)	Cooling rate (°C min^{-1})	η stabilisation T_{Stab}, time (°C), (h)	Cooling rate (°C min^{-1})	Ageing temp., time (°C), (h)
DT706_1	1080, 2	4	835, 10	20	—
DT706_4	1080, 2	0.5	835, 10	20	—
DT706_2	1080, 2	20	835, 10	20	—
6-1	1080, 3	2.3	832, 10		720, 8
6-2	1080, 3	5	940, 10		—
6-3	1080, 3	5	920, 10		—

The experimental polycrystalline Ni–Fe-based superalloy DT706 used in the present study is derived from the commercial Inconel 706 alloy and was developed for disk application in steam turbines for use at temperatures above 700 °C. The development of DT 706 alloy was aimed at improving the microstructural stability of Inconel 706, while preserving its excellent manufacturability and good mechanical properties. In 706-type alloys, the properties depend directly on the precipitation hardening system, which is based on the coherent precipitation of two kinds of A_3B-type compounds. The austenitic matrix (γ phase) is strengthened by the precipitation of extremely fine, coherent and ordered Ni_3X-type intermetallic phase compounds of γ' (fcc $L1_2$ crystal structure, X = Al) and γ'' (bct DO_{22} structure, X = Nb) phases. In both γ' and γ'' phases the X atom can be partially substituted by other elements (mainly Al, Nb, Ti), so that the real compositions of the two intermetallics are more complex: the fcc Ni_3Al[Ti, Nb] γ' phase and the bct Ni_3Nb[Ti] γ'' phase.

Although all the Ni_3X-type phases have different crystal structures, they actually involve different stacking of the close-packed planes where the atoms are arranged in alternate rows of A–A and A–B atoms [2]. Since the close-packed planes are also the principal slip planes, the passage of a dislocation can disrupt the stacking sequence and therefore locally form a nucleus of a different crystal structure. For instance, a fault in the metastable $L1_2$ structure (γ') phase represents a nucleus of the stable DO_{24} η phase. Further, the transition from one phase to the other is affected by the affinity for different chemical species in the γ', γ'' and η phases. In Inconel 706 the γ' and γ'' precipitates exhibit a metastable character and transform to large laths of η phase (hcp Ni_3Ti[Nb]) upon exposure to temperatures above 700 °C. This overageing process is accompanied by an unacceptable loss of creep and tensile strength. In order to overcome this impasse, the [Ti + Al]/[Nb] ratio of Inconel 706 was specifically refined in order to minimise the thermodynamic tendency for the transformation of γ'/γ''. This modification was associated with a redesign of the Inconel 706 chemistry, resulting in the new alloy, named DT706.

It may be noted here that the γ'' precipitates in 706-type alloys are often associated with the γ' phase, as the $L1_2$ particles (γ') are potential nucleation sites for the DO_{22} phase (γ''). Thus, along with the single-phase γ' and γ'' particles, a combined form of the two precipitates, the so-called 'co-precipitates', may also be present in the microstructure, depending on the heat-treatment conditions. Different morphologies of co-precipitates have been reported in the literature by Cozar and Pineau [3]. Due to all these features, the microstructure of DT706 is rather complex.

The present paper deals with the microstructural characterisation and heat-treatment optimisation of DT706 alloy with the help of *in situ* heating experiments in small-angle neutron scattering (SANS). The complex microstructure and the lack of information about DT706 alloy make the characterisation of the precipitation behaviour a very intensive and challenging work. It was therefore performed by combining two complementary investigation techniques: i.e. conventional microstructural examination by scanning and transmission electron microscopy (SEM and TEM) plus neutron scattering at small angles. *In situ* SANS results were evaluated with the help of microstructural characterisation of differently heat-treated samples and comparing with *ex situ* SANS measurements previously performed on DT706 [4] and Inconel 706 [5] alloys.

2. Experimental details

The nominal composition of DT 706 alloy is 22% Fe, 18% Cr, 3% Nb, 1.9% Ti, 0.55% Al, and 0.01% C, and the rest is Ni (in wt%). The alloy was prepared by vacuum induction melting (VIM), vacuum arc refining (VAR) and forging to a bar shape. The samples cut from the bar were subjected to a three-step modified stabilisation treatment (MST) that was adopted from Inconel 706 alloy [6]. The heat treatment cycle consists of a solution treatment (T_{sol}) step at 1080 °C for 3 h and an η stabilisation (T_{stab}) step at 835 °C for 10 h, followed by an ageing step at 720 °C for 8 h. The samples were slowly cooled at 4 °C min^{-1} from the solution temperature to the η stabilisation temperature. The microstructure after the MST heat treatment is shown in figure 1, which shows the presence of γ'/γ'' co-precipitates. However, for the evaluation of data for *in situ* SANS measurements, it is important to note that the γ'' phase does not form above 800 °C.

In the *in situ* heating cycles for the SANS measurements—(i) the η stabilisation temperature (T_{stab}) was varied (835,[6] 920 and 940 °C) and (ii) the cooling rate from the solution to the η stabilisation temperature was varied (20, 4, 2.3 and 0.5 °C min^{-1}). The different *in situ* samples are listed in table 1.

[6] The actual η stabilisation temperature for the *in situ* cycle at HMI was 832 °C instead of 835 °C in the MST heat treatment, which was also used in the measurements at PSI.

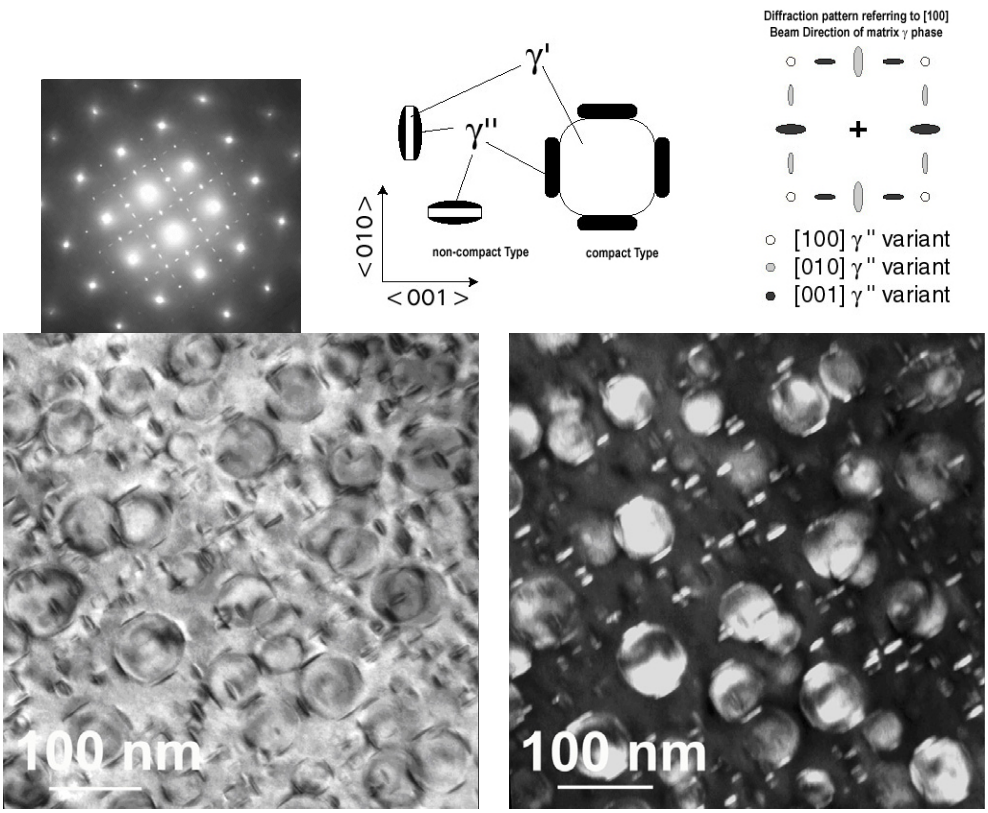

Figure 1. γ'/γ'' co-precipitates after MST heat treatments. TEM images; bright field (a) / dark field (b) pair and selected area diffraction pattern. The inset shows a schematic representation of the co-precipitate structure and the superlattice diffraction spots from the different variants of the γ'' precipitates.

Neutron scattering measurements were carried out at the SANS II instrument of the SINQ user lab of the Paul Scherrer Institute (PSI), Villigen, Switzerland [7] and at the V4 instrument of the BENSC facility at the Hahn Meitner Institute, Berlin (HMI), Germany [8]. Samples in the form of platelets (12 mm × 12 mm × 2 mm) were measured and a standard Institut Laue-Langevin (ILL)-type vacuum furnace was used for the *in situ* heating. The scattering data were collected at several geometries; the sample-to-detector distance, SDD, varied from 1 to 16 m and the neutron wavelength, λ, varied from 4.55 to 19.6 Å. The covered range of the scattering vector magnitude, $Q = |\mathbf{Q}|$, was approximately 2×10^{-3} to 0.1 Å^{-1} (i.e. 2×10^{-2} nm^{-1} $< Q <$ 1 nm^{-1}), where the magnitude $Q = |\mathbf{Q}| = |\mathbf{k} - \mathbf{k}_0|$, with $\mathbf{k}_0$ and $\mathbf{k}$ being the wavevectors of the incident and scattered neutrons, respectively, and $|\mathbf{k}| = |\mathbf{k}_0| = 2\pi/\lambda$ due to the elastic scattering. The measured raw data were corrected for background scattering and calibrated to the absolute scale.

The scattered intensity of the neutrons is proportional to the volume fraction, as well as to the scattering contrast $(\Delta\rho)^2$ (i.e. the square of the difference between scattering-length densities (SLD) of the precipitate and matrix phases, see e.g. [9]). The SLD of the individual phases depends on their composition, which is not known precisely for the DT706 alloy at different temperatures. Therefore, the quantity, which is reported later in the text, is 'volume fraction times the scattering contrast' and only the relative evolution of the volume fraction could thus be deduced in the present study.

The precipitate microstructures were also studied using scanning and transmission electron microscopy. Specimens for scanning electron microscopy were prepared by conventional mechanical grinding and polishing. All samples were etched with the 'V2A-Beize' mixture [10] at a temperature between 60 and 70 °C. Foils for transmission electron microscopy were cut, punched to 3 mm diameter and twin jet-polished at −15 °C with a solution of 30 ml ethyleneglycol monobutyl ether, 63 ml ethanol and 7 ml $HClO_4$. A Leo 1550 Gemini SEM with a field-emission gun and an in-lens detector having a point-to-point resolution of 3 nm and a Philips CM 12 TEM operating at an accelerating voltage of 120 kV was used for microstructural studies.

3. Model

The *in situ* SANS results were used to calculate the microstructural parameters of the γ' and η phase precipitates mainly during the temperature decrease $T_{\text{sol}} \rightarrow T_{\text{stab}}$ and during a hold at T_{stab}. Collected scattering data were processed with an analysis technique developed by Strunz *et al* [11] based on the simulation of a scattering profile generated from a three-dimensional (3D) microstructural model of a particle system. Here, the modelled scattering curve also contained the interparticle interference effect. The calculated profile is

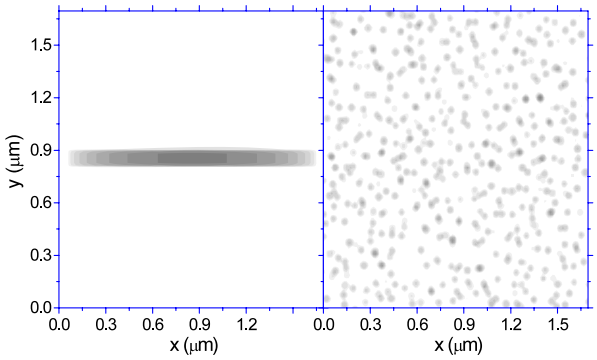

Figure 2. The projection of 3D models of precipitates—η (left) and γ' (right).

matched (by computer simulation) with the experimental curve in order to find the microstructural parameters (i.e. the size and the centre-to-centre distance of the γ' particles) which best fit the experimental data. The model that was used approximated the γ' precipitate by a spherical shape, in agreement with the indication obtained from the TEM image analysis. As the γ'' precipitates are not present at T_{stab} and above, they are not considered here.

Two models were fitted to the measured data at the same time (figure 2):

(1) The η phase was modelled as plate-like particle with a fixed plate thickness (figure 2, left).
(2) The γ' precipitates were modelled as spherical particles with a lognormal size distribution (figure 2, right).

The size and the thickness of the η phase plates were estimated from SEM micrographs and also from the average value obtained by the pre-fitting of SANS data. The plate thickness was fixed at 900 Å. For all calculations the η plates are relatively large, so that they contributed only to the low Q-range. They contributed to the scattering at most (when compared with other contributions) in the Q-range 0.002–0.004 Å^{-1}. For the evaluation it was assumed that the thickness of η does not change during the thermal history.

The modelling of the γ' phase showed that its volume fraction at the η stabilisation temperature should be relatively low (12% at maximum) because, for a larger volume fraction, an interparticle interference peak would be observed otherwise. The information obtained on distance is thus not unambiguous. The geometrical (local) volume fraction of the γ' precipitate model was thus fixed at 6%. This estimate is the average value obtained from the data after long hold times at the η stabilisation temperature (835 °C). For this condition the highest volume fractions of γ' were determined during the pre-fitting, considering unconstrained precipitate distances.

The fixing the volume fraction of the γ' phase while holding at elevated temperatures agrees with the Oswald ripening mechanism of precipitate coarsening [12]. However, the geometrical volume fraction of the model was not fixed for the fits performed on the data measured while decreasing temperature from the solution temperature to T_{stab} and also just after the fast cooling (20 °C min^{-1}). It is assumed that the γ' volume fraction does not reach equilibrium instantaneously, but needs a short time for this after the fast cooling. In accordance with the Oswald ripening mechanism, it was also assumed that the composition of the precipitates, and thus their SLD and consequently the scattering contrast, does not change during the hold period at T_{stab}. Although the precise scattering contrast is not known, it is assumed to be constant at T_{stab}. This enables relative determination of the evolution of the total volume fraction of the precipitates.

The output parameters from the fit are the γ' precipitate size, its relative volume fraction (relative only since the absolute value of the scattering contrast is unknown) and the relative volume fraction of the η plates.

4. Results

The *in situ* heating cycle for the SANS measurements mainly studied the effect of cooling from the solution temperature to the η stabilisation temperature and the effect of the η stabilisation temperature on the precipitation of the η and γ' phases. By combining the results of experiments carried out at PSI and HMI at three different η stabilisation temperatures and four different cooling rates from the solution treatment to T_{stab} (see table 1), it was possible to monitor not only the precipitation behaviour of the two phases but also, to some extent, the phase transformation from the γ' to η phases.

4.1. Different η stabilisation temperatures

The *in situ* heating cycle included heating to the solution temperature, cooling down to the η stabilisation temperature, and finally cooling down to room temperature (RT) after holding at different T_{stab} temperatures (figure 3(a)). SANS spectra were obtained at different points (marked by circles in figure 3(a)) in the heating cycle. The scattering measured at different T_{stab} temperatures in two of the samples (nos 6-1 and 6-2) are shown in figures 3(b) and (c), respectively. The scattering curves from sample 6-3 ($T_{\text{stab}} = 920$ °C) show similar behaviour to that in sample 6-2 ($T_{\text{stab}} = 940$ °C) and are therefore not presented separately. The plots in figure 3 also include scattering measured at RT after completion of the *in situ* heating cycles. Practically no precipitation is observed at the higher η stabilisation temperatures of 920 and 940 °C. At these temperatures, the scattering comes only from large inhomogeneities like carbides, which also scatter at the higher solution treatment temperature. The carbide solution temperature must therefore be much higher than 1080 °C. However, the two *in situ* cycles with T_{stab} at 920 and 940 °C provided important information that there was no precipitation of either η or γ' at these temperatures. In these cycles, fine precipitates are produced only on fast cooling down to room temperature from T_{stab} (figure 3(b)). In contrast, the scattering profiles from T_{stab} at 832 °C (figure 3(c)) show precipitation, which can be observed from the intensity increase with respect to the solution-temperature measurement, in the broad Q-range (0.004–0.06 Å^{-1}). Additionally, new precipitation occurs during ageing at 720 °C (see figure 3, Q-range 0.02–0.05 Å^{-1}). Either a small secondary γ' phase precipitates or a mantle of γ'' on the existing γ' precipitates is formed to produce the co-precipitates.

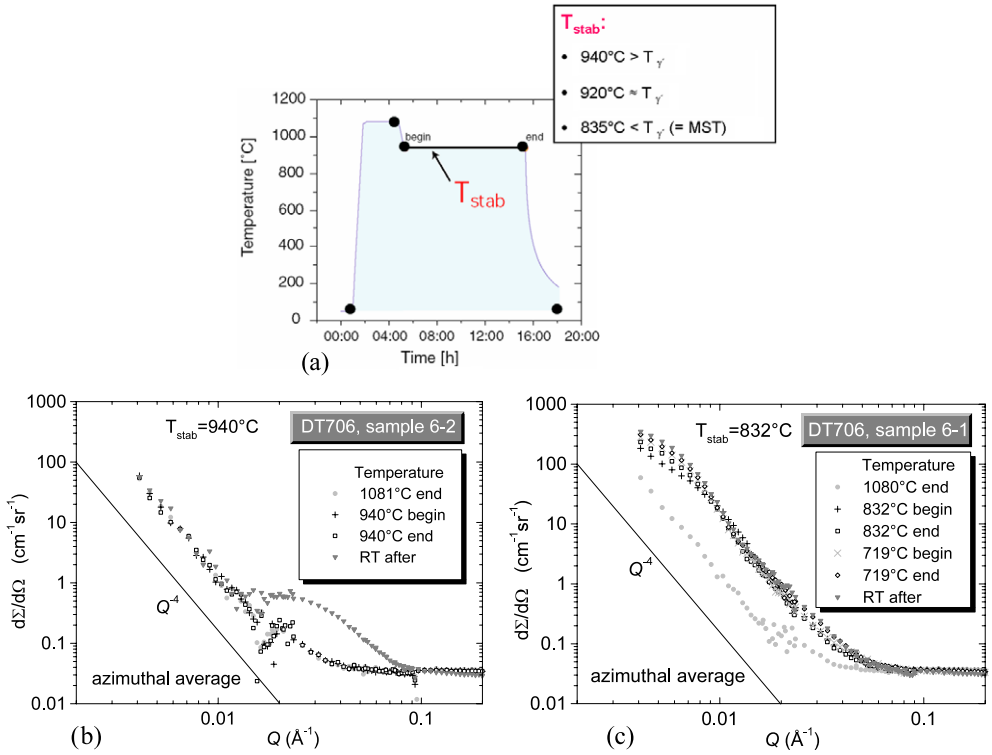

Figure 3. The measured scattering cross section as a function of Q, obtained by azimuthal averaging of the two-dimensional isotropic scattering profiles at different temperatures of the *in situ* samples ($T_{\text{stab}} = 940$ and 832 °C).

4.2. Different cooling rates from solution temperatures

In addition to the samples treated at different η stabilisation temperatures, *in situ* SANS measurements were also performed on heating cycles with varying cooling rates from the solution temperature to the η stabilisation temperature. For a better understanding of the evolution of precipitation, the dependence of the integral scattering intensities at three different cooling rates are plotted together with the thermal history in figure 4. The integral intensity collected by the detector for a fixed SDD (5 m) and wavelength (4.55 Å) is used to present the nucleation and growth of γ' and η precipitates. For these *in situ* cycles, $T_{\text{stab}} = 835$ °C was selected.

The observed increase in integral intensity on cooling to RT after the hold at 835 °C (figure 4) is rather surprising. Moreover, when displayed in a temperature–intensity plot, this increase is nearly linear with the temperature change. In the low-temperature region (below 700 °C) no significant precipitation is expected. Further, at these relatively low temperatures, diffusion is slow and therefore no significant composition change in the matrix and the precipitate phases are likely. An explanation for the increase in intensity could be the different thermal expansion coefficients of the matrix and the precipitate, resulting in a slightly different evolution of their lattice constants (and thus the unit cell volume) with temperature. This small difference is actually large enough to cause a change in the scattering contrast of γ', as well as η. This effect is, however, conditional on only a small difference in the matrix and precipitate SLDs due to the composition. This feature, which can in principle be used for the determination of the temperature dependence of the lattice misfit, will be the subject of a separate paper and therefore not discussed further in this text. Here we deal predominantly with the high-temperature measurements.

For the intermediate cooling rate (4 °C min^{-1}) the precipitation begins already at 852 °C (figure 4(b)), even before the stabilisation temperature of 835 °C is reached. This behaviour is quite different in the 20 °C min^{-1} cooling rate sample (figure 4(a)), which shows that precipitation starts during the 835 °C hold and not before. It thus indicates that the precipitation strongly depends on cooling rate from T_{sol} to T_{stab}. For the fast cooling rate (20 °C min^{-1}), the integral intensity reaches saturation only at the end of the holding at 835 °C. However, in the case of the intermediate cooling rate (4 °C min^{-1}) a sharp increase in the intensity commences at the last stage of the temperature decrease (i.e. below 852 °C) and the integral intensity saturates quickly at T_{stab}. The increase in intensity is actually caused by nucleation of both γ' and η precipitates. The kinetics of the phase transformations (both γ to γ' and γ to η) at the intermediate cooling rate seem to be fast enough to produce precipitates in high volume fraction, corresponding to the equilibrium fraction at each temperatures. The integral intensity reaches saturation very quickly at a relatively high level within 3 h of holding at 835 °C (figure 4(b)). This increase in intensity is mainly due to the increase in the precipitate size while the precipitate volume fraction remains constant (Ostwald ripening).

At the slowest cooling rate (0.5 °C min^{-1}) precipitation already starts before the hold temperature of 835 °C is reached during cooling from T_{sol}. In fact, the integral intensity tends

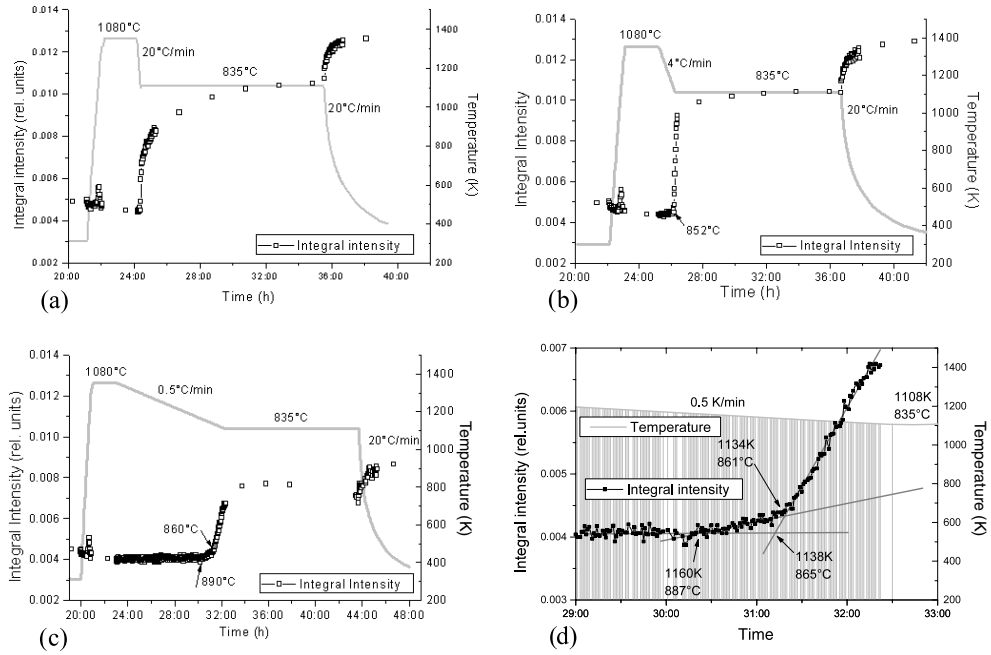

Figure 4. Integral intensities on the detector (SDD = 5 m, $\lambda = 4.55$ Å) as a function of temperature, for the *in situ* heating cycle with varying cooling rates from T_{sol} to T_{stab}: (a) 20 °C min^{-1}; (b) 4 °C min^{-1}; (c) 0.5 °C min^{-1}. (d) Enlargement of the critical region in (c).

to increase, starting at 890 °C (figure 4(c)). Most likely, this increase corresponds to the start of η precipitation. The increase in integral intensity further accelerates at 865 °C and this is interpreted as the onset of γ' precipitation. This division is clearly visible when the corresponding temperature region in figure 4(c) is zoomed (see figure 4(d)). This result was employed for the separation of scattering from η and γ'.

The precipitates grow to large size, already during the slow temperature decrease from T_{sol} to T_{stab} (nearly similar to size, corresponding to the ageing behaviour observed during the hold at 835 °C in the other two *in situ* cycles with faster cooling). The integral intensity, however, did not reach such high values as in the case of the faster-cooled samples. It is obvious that the highest scattering intensity per precipitate (corresponding to a specific size) in the Q-window used for monitoring the integral intensity was reached already at a higher temperature, where a relatively low volume fraction of γ' precipitates was still present. On holding at the η stabilisation temperature (835 °C), a fast saturation of the intensity at a low level is visible. Also, a tendency for a decrease in the integral intensity in the last part of the holding time is observed (figure 4(c)). There is, in fact, movement of the scattered intensity towards still smaller Q-values due to the increased precipitate size. The scattered intensity is thus disappearing from the given Q-range over which the integration was performed.

4.3. Scattering curves

As mentioned earlier, there is always (i.e. even at the solution treatment temperature) scattering from large inhomogeneities, most probably from carbides which are also visible in SEM. This forms the base scattering (Porod-law shape) and the scattering from the γ' and η phases is superimposed on this. For data evaluation this is particularly taken care of by first evaluating the scattering curves measured at the solution treatment temperature, and the resulting modelled scattering curve was later used as a pad under the modelled scattering from the η and γ' precipitates.

As can be seen from figures 3(c) and 5, the scattering evolves in different ways for the *in situ* cycles involving the four cooling rates (three samples measured at PSI and one at HMI). Representative microstructures from the three samples measured at PSI, after the complete *in situ* cycle, are shown in figure 6. The γ' precipitate microstructures from the fast-(20 °C min^{-1}) and intermediate-cooled (4 °C min^{-1}) samples look quite similar, however the scatterings evolved very differently for different conditions of cooling from T_{sol} (1080 °C) to T_{stab} (835 °C), as can be seen from figures 5(a) and (b). In both cases, the γ' precipitates are a dense system of small spheres of size much smaller than 100 nm. In contrast, in the slowly cooled sample (0.5 °C min^{-1}), the scattering from η is practically masked by scattering from γ' during the hold at 835 °C because the γ' precipitates are already very large and scattering to the same Q-region as η. A tendency for γ' to η transformation is clearly visible in figures 6(c) and (d), which shows that first the γ' precipitates align along the the [110] crystallographic direction and later transform to η plates. The γ' precipitates are also coarser in this sample than in the case of faster cooling rates, which also get reflected in the scattering curves (figure 5(c)).

5. Evaluation and discussion

A dependence of the model parameters on time and temperature at the elevated temperatures was realized during the evaluation of the SANS data.

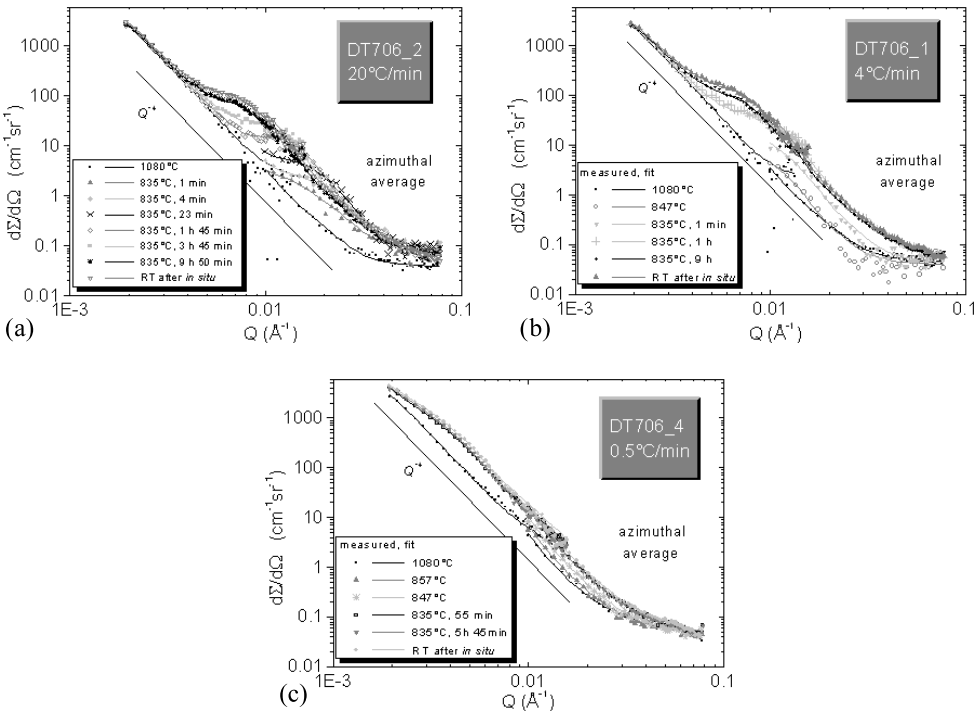

Figure 5. Evolution of scattering curves with hold time at the η stabilisation temperature (835 °C).

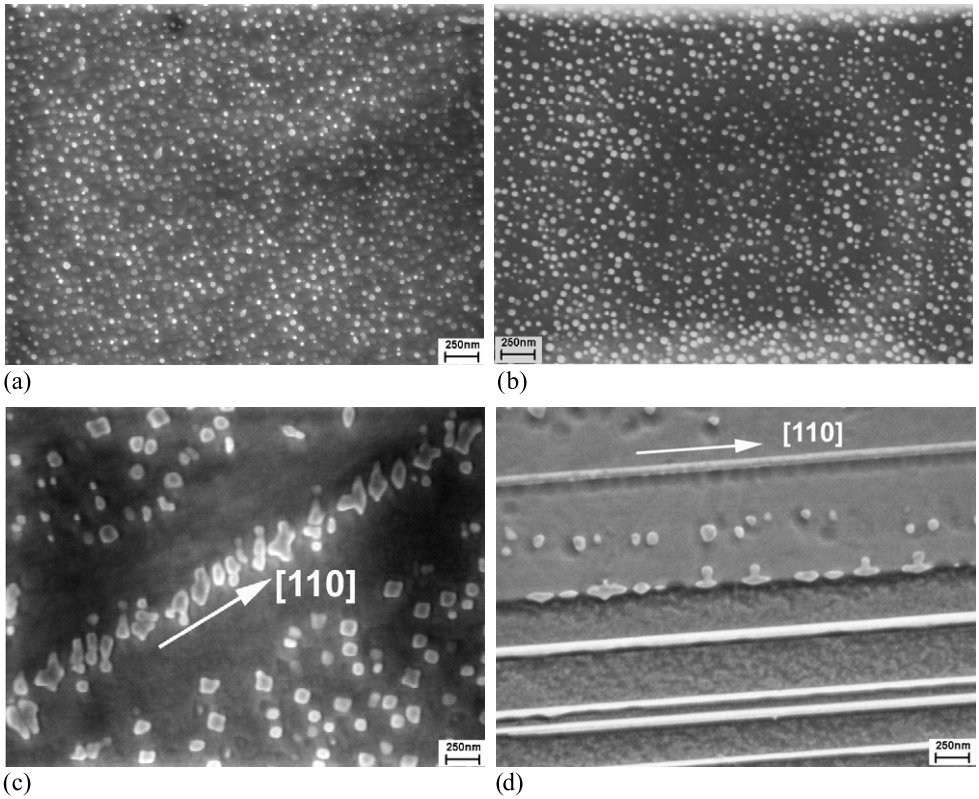

Figure 6. SEM micrographs of *in situ* samples with varying cooling rates after the complete heating cycle: (a) 20 °C min^{-1}; (b) 4 °C min^{-1}; (c) and (d) 0.5 °C min^{-1}.

5.1. Size of γ' precipitates

Figure 7 shows the size evolution of the γ' precipitates during holding at T_{stab} after the different cooling cycle from T_{sol}. The approximate initial (i.e. just after the temperature decrease to T_{stab}) and final (10 h hold) mean precipitate sizes of the four *in situ* cycles are reported in table 2.

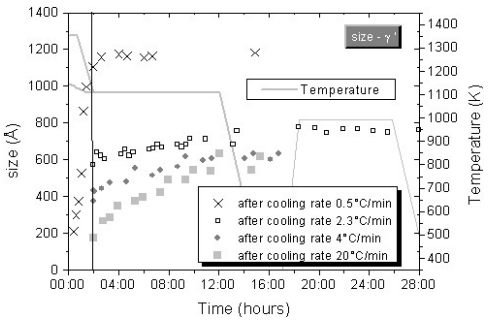

Figure 7. Evolution of mean size of γ' precipitates during holding at a η stabilization temperature around 835 °C.

Table 2. γ' precipitate size evolution during holding at the η stabilisation temperature (835 °C) on samples cooled at different rates from the solution temperature.

Sample no.	Cooling rate (°C min^{-1})	Size hold begin (nm)	Size hold end (nm)
DT706_2	20	18	58
DT706_1	4	41	61
6-1	2.3	60	72
DT706_4	0.5	110	120

The scattering curves during the temperature decrease were measured always in the large-Q geometry only (SDD 5 m, wavelength 4.55 Å), i.e. at the geometry at which the evolution of the η precipitate size cannot be assessed because its Q-range is too large to recognize any shape of the scattering curve from η above the background in the temperature region 890–865 °C (i.e. only the integral intensity change can be observed here, as done in figure 4(d)). On the other hand, the γ' scattering at large Q-magnitudes could be used for the precipitate size evaluation during the slow temperature decrease in the range 865–845 °C.

It can be observed from figure 7 that there is a significant dependence of the γ' size evolution during hold at 835 °C on the prior cooling history. Generally, the faster the cooling, the smaller is the precipitate size at the beginning of the hold at T_{stab}. Moreover, a broader γ' size distribution is obtained when the cooling is very slow. This is understandable, as precipitates nucleate over the broad temperature range during the significant time span that the sample spends at each temperature during slow cooling. The precipitates that nucleate at the higher temperatures thus grow at lower temperatures where new ones have also just formed.

However, it may be noted that fast cooling from T_{stab} to RT after the hold does not change the precipitate size. A similar conclusion can be speculated for the sample 6-1 after further ageing (heating to 720 °C and 8 h hold), although the result here could already be influenced by a fresh precipitation (small γ' or even γ'') observed at very large Q-magnitudes (figure 3(c) and section 4.1). This precipitation was not included in the model that was used for the SANS data evaluation.

5.2. Volume fraction of γ' and η

Figure 8 displays the evolution of volume fraction times the scattering contrast for the *in situ* cycle with various cooling rates. It is observed that the change in scattering contrast always occurs on cooling to RT after the 835 °C hold. This increase is a result of the difference in thermal expansion coefficients of the precipitate and matrix phases, as explained above in section 4.2. This effect causes a step-like increase in

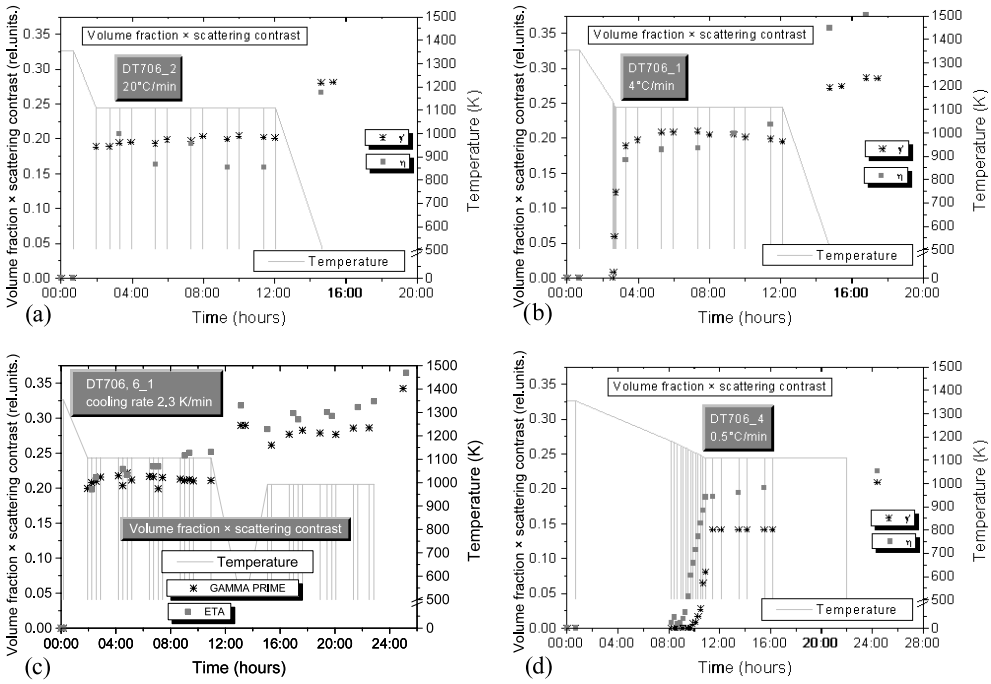

Figure 8. Volume fraction times the scattering contrast evolution after different cooling rates from T_{sol} to T_{stab} for both γ' and η: (a) 20 °C min^{-1}; (b) 4 °C min^{-1}; (c) 2.3 °C min^{-1}; (d) 0.5 °C min^{-1}.

the global volume fraction times the scattering contrast after cooling to RT, as seen in figures 8(a)–(d).

For the sample with slow cooling from T_{sol} to T_{stab}, a separation (sudden jump) in the scattering is seen according to the integral intensity evolution: it is assumed that the η precipitation starts at around 887 °C (detailed plot in figure 4(d)). The integral intensity accelerates its increase (at 865 °C—figure 4(d)) and it is assumed that γ' precipitation also starts at this point. Below 865 °C, η precipitation together with γ' has to be considered, but the latter scatters dominantly. The η precipitate volume fraction is extrapolated in this region from the data obtained above 865 °C. On holding at 835 °C the γ' fraction becomes very large and the scattering form η cannot be separated unambiguously from the γ' scattering. No direct conclusions can thus be made on the η and γ' volume-fraction evolution after slow cooling. Here, the γ' volume fraction during the hold is approximated by a constant value in the evaluation (Oswald ripening case). Doing so, the modelled η volume fraction increases (see figure 8(d)). This indicates that the transformation γ' to η cannot be excluded here.

Intermediately after fast cooling, there is an indication that the volume fraction times the scattering contrast of γ' actually decreases during the hold at 835 °C. At the same time, the volume fraction of η increases (see figures 8(b) and (c)). A tendency of the transformation of γ' to η for this type of cooling can therefore be concluded. The volume fraction scale in figure 8 is relative (because of the scattering contrast uncertainty) and, moreover, is different for the two phases (they are put in the same plot in order to compare the tendencies). Therefore, it is not possible to make a simple summation of the two volume fractions. As γ' is the dominant phase, its transformation to η, even when in a small amount, can make a significant change in the η volume fraction.

The evolution of the precipitate volume fraction is different in the fast-cooled samples (20 °C min^{-1}) compared to the intermediately fast-cooled sample (4 °C min^{-1}). On holding at 835 °C, a decrease in the γ' volume fraction is not observed. Nor is any tendency for a η volume-fraction increase observed. The γ' size is small (<60 nm even after a 10 h hold at T_{stab}) after fast cooling. Apparently, a critical γ' precipitate size must be reached before it can transform to η. However, no comments on the critical composition of the γ' phase for transformation to η can be made from the present study. Since γ' is Al rich and η is Ti rich, a partitioning of elements, at least in the close vicinity of the transforming precipitates, does occur. This change in the microchemistry is indirectly visible in figures 6(c) and (d), reflected through the precipitate-free zone in the vicinity of transforming η plates (figure 6(c)). An associated change in the SLD was not easy to separate from the effect of the change in volume fraction that also occurs simultaneously.

6. Conclusions

The evolution of γ' size for various cooling rates and hold times can be extrapolated and the microstructure of DT706 alloy can be tuned using these results. It is apparent that the cooling rate from T_{sol} to T_{stab} is a critical parameter in the heat treatment of the alloy and has to be appropriately chosen and accurately controlled during the heat treatment.

Although the scattering from the η phase gives only a small intensity increase above the background scattering from carbides, there is a clear indication of an increase in the η amount (at the expense of γ') on holding after the intermediately fast cooling. The same tendency is also expected after the slow cooling, and electron microscopy observation supports this. In the present *in situ* SANS results, this is not obvious but cannot be excluded. On the other hand, such a transformation tendency is not observed in the SANS data after fast cooling.

Using *in situ* slow cooling, the start temperature of both the η (887 °C) and γ' (865 °C) precipitations could be determined precisely. These values generally agree with thermodynamical calculations using the Thermocalc software.

Acknowledgments

The authors are indebted to BENSC (HMI Berlin) and SINQ (PSI Villigen) for providing the beam time at the SANS facilities. The travel support to P Strunz for the experiment at PSI in the frame of the 6th Framework Programme 'Strengthening the European Research Area, Research Infrastructures'—contract no. RII3-CT-2003-505925 (NMI3)—is acknowledged as well. P Strunz also acknowledges the support of the MSM2672244501 project.

References

[1] Rösler J, Müller S, Del Genovese D and Götting M 2001 Design of Inconel 706 for improved creep crack growth resistance *Superalloys 718, 625, 706 and Various Derivatives* (Warrendale, PA: TMS) pp 523–34
[2] Durand-Charre M 1997 *The Microstructure of Superalloys* (Boca-Raton, FL: CRC Press) p 47
[3] Cozar R and Pineau A 1973 *Metall. Trans.* A **4** 47–59
[4] Del Genovese D, Strunz P, Mukherji D, Gilles R and Rösler 2005 *J. Metall. Mater. Trans.* **36A** 3439–50
[5] Mukherji D, Strunz P, Del Genovese D, Gilles R, Rösler J and Wiedenmann A 2003 *Metall. Mater. Trans.* **34A** 2781–92
[6] Müller S and Rösler J 1999 *Life Assessment of Hot Section Gas Turbine Components* ed R Townsend, M Winstone, M Henderson, J R Nichols, A Partridge, B Nath, M Wood and R Viswanathan (Cambridge: Cambridge University Press) pp 49–60
[7] Strunz P, Mortensen K and Janssen S 2004 *Physica* B **350** e783–5
[8] Keiderling U and Wiedenmann A 1995 *Physica* B **213/214** 895–7
[9] Kostorz G 1979 *Neutron Scattering (Treatise on Materials Science and Technology)* ed G Kostorz (New York: Academic) pp 227–89
[10] Günter P 1994 *Metallographisches, Keramographisches, Plastographisches Ätzen* (Berlin: Gebrüder Bornträger) p 241
[11] Strunz P, Gilles R, Mukherji D and Wiedenmann A 2003 *J. Appl. Crystallogr.* **36** 854–9
[12] Doi M 1996 *Prog. Mater. Sci.* **40** 79–180